A 36-base hairpin within lncRNA *DRAIC*, modulated by alternative splicing, interacts with the IKKα coiled-coil domain and inhibits NF-κB and tumor cell phenotypes.

Running Title: 36-Base Hairpin of DRAIC

Xiaoxiao Hao[1], Yuechuan Chen[1], Divya Sahu[1], Róża K. Przanowska[3], Chase A. Weidmann[4], Isaac Nardi[2], Kevin M. Weeks[5], Anindya Dutta[1, 6]

[1]University of Alabama at Birmingham, Department of Genetics, Birmingham, AL,

[2]NardiLabs, Miami, FL,

[3]University of Virginia, Department of Biochemistry and Molecular Genetics, Charlottesville, VA,

[4]Department of Biological Chemistry, Center for RNA Biomedicine, Rogel Cancer Center, University of Michigan Medical School, Ann Arbor, MI

[5]Department of Chemistry, University of North Carolina, Chapel Hill, NC

[6]Corresponding author

Keywords: long non-coding RNA DRAIC, SHAPE-MaP, IKK complex, NF-κB signaling pathway and Surface plasmon resonance (SPR)

Abstract

The 1.7 kb DRAIC long noncoding RNA inhibits tumor growth, inhibits cancer cell invasion, migration, colony formation and interacts with IKK (IκB kinase) subunits, inhibiting the phosphorylation and degradation of the NF-κB inhibitor, IκB, to suppress the activation of NF-κB. Whether these activities are all linked is unclear. We used SHAPE-MaP to obtain the secondary structure of the lncRNA to perform structure-functions studies which identified the minimal region of DRAIC necessary for repressing NF-κB. A 36-nucleotide hairpin (A+B) within DRAIC inhibits NF-κB, inhibits IκB phosphorylation and binds specifically with the IKKα coiled-coil domain with a very high affinity: K_D of ~1-5 nM. This interaction weakens the dimerization of of the coiled coil domains of two IKK subunits, a dimerization that is indispensable for IKK activity. A+B is sufficient and necessary to inhibit the oncogenic phenotypes in multiple cancer cell-lines, demonstrating that interaction with IKK and inhibition of NF-κB is key for cancer suppression by DRAIC. Presence of this critical hairpin is modulated by alternative splicing the extends exon 4 to exon 4a of DRAIC and the expression of exon 4a in lung tumors is associated with low NF-κB activity. This is also the first demonstration that a short RNA can disrupt coiled-coil dimerization.

Introduction

Long non-coding RNAs (lncRNAs) are emerging as significant regulators of gene expression, implicated in a variety of cellular processes including cancer progression [1, 2]. Unlike protein-coding genes, lncRNAs do not translate into proteins but instead exert their functions through interactions with DNA, RNA, or proteins [3, 4]. The down-regulated lncRNA in cancers (DRAIC) has been previously identified as inhibiting tumorigenic phenotypes [5-8]. Our prior studies demonstrated that DRAIC inhibits the activation of NF-κB, a transcription factor known for its role in promoting cancer cell survival, proliferation, and metastasis [5]. This inhibition is mediated through the disruption of the IκB kinase (IKK) complex, which comprises the catalytic subunits IKKα and IKKβ, and the regulatory subunit IKKγ (also termed NEMO, NF-κB Essential Modulator) [5, 9]. However, it is unclear how the lncRNA DRAIC interacts with IKK. DRAIC expression predicts good outcomes in multiple different cancer types [5, 6, 10, 11], highlighting the need to define the precise mechanisms underlying its role.

We previously showed that the functional regions of DRAIC responsible for interaction with IKKα lie within positions 705-950 of DRAIC [5]. Here we define exactly the region within this 200 nt segment of DRAIC that interacts with its target IKK to demonstrate whether the cell biological effect segregates exactly with the biochemical function of the RNA. Pinpointing the exact interaction region within the lncRNA and the corresponding amino acids in the target protein is crucial for understanding its molecular mechanism, for definitively demonstrating that the biochemical activity of the lncRNA is responsible for its anti-cancer effect and for potential therapeutic applications.

In this study, we used SHAPE-MaP-based structure prediction, followed by structure-function analysis to pinpoint the minimal functional region of DRAIC responsible for its interaction with IKK and subsequent inhibition of NF-κB activity. A hairpin structure within DRAIC,

encompassing nucleotides 705-722/741-758 (termed A+B), is critical for this interaction. This region effectively suppresses cancer cell invasion, migration, and clonogenicity by physically interacting with IKKα and thus inhibiting NF-κB activity. By defining the specific interaction region of DRAIC and its target, our findings reveal a direct mechanism through which a lncRNA regulates key cancer pathways, positioning DRAIC as a potential therapeutic molecule for cancer treatment. This critical region of DRAIC is contained in an alternatively spliced exon, the inclusion or exclusion of which regulates NF-κB driven gene expression in lung adenocarcinomas. Finally, this is the first demonstration that a short RNA can disrupt dimerization mediated by coiled-coil domains, identifying a novel tool for therapeutically disrupting such interaction in myriad areas of cell biology.

Results

SHAPE-MaP informed modeling of DRAIC RNA structure

To identify functional motifs within the DRAIC RNA, we chemically probed the RNA structure of DRAIC RNA extracted from cells with the SHAPE reagent 5NIA. To identify SHAPE-reactive nucleotides, we employed mutational profiling reverse transcription (MaP-RT), where SHAPE-modified nucleotides trigger skipping or random nucleotide addition in product cDNA, and these "mutation" events can be measured by sequencing. MaP cDNA amplicons generated by SuperScript II RT are on average ~500 nucleotides in length, so we targeted our initial MaP experiments to the functional part of DRAIC (705-950 bp), ultimately amplifying DRAIC nts 655-1132 and measuring SHAPE reactivity for nts 677-1107. We modeled the RNA structure of DRAIC including our SHAPE reactivity as added restraints [12-14] (**Fig. 1**). We discovered three very well-determined RNA structures within the active region (modeled pairing probabilities > 95 %, **Fig. 1**) that we considered for functional elaboration, including a multi-bulge-containing duplex containing regions we termed A, B, and C (**Fig. 1**). While this ABC region is among the

most well-determined in our model, high SHAPE reactivity in stem A suggests that this structure may be somewhat intrinsically flexible, at least in the absence of proteins and other macromolecules.

A 36-region hairpin containing nucleotides 705-722/741-758 (A+B) within DRAIC is sufficient and indispensable to inhibit NF-κB activity

We dissected DRAIC into several fragments based on the modeled secondary structure and used NF-κB luciferase reporter assays to identify the regions responsible for inhibiting NF-κB activity (**Fig. 2A**). Consistent with our published data, we found that both the full-length (FL) DRAIC and the 705-950 fragment significantly inhibit NF-κB activity compared to the empty vector (EV) and a 900-1705 fragment of DRAIC [5]. When we systematically truncated the 705-950 region of DRAIC, we discovered that the ABC region (nts 705-758) was sufficient for inhibiting NF-κB. Further deletions within the sufficient ABC construct revealed that the C portion of the hairpin (nts 722-741) is not necessary for the inhibition, and regions A and B expressed as a single fused hairpin maintained full activity. All constructions containing the natural A+B sequence, as well as the fused A+B hairpin alone, showed significant inhibition of NF-κB activity in three different cell lines (**Fig. 2B**). This suggests that the A+B hairpin is responsible for the inhibitory effect of DRAIC.

As expected, deletion of A and B sequence from the original functional region of DRAIC (nts 705-950) abolished repression in three cell lines (**Fig. 2C**). This demonstrates that the A+B hairpin structure is both necessary and sufficient for the suppression of NF-κB activity.

A+B selectively interacts physically with IKKα, but not NEMO or IKKβ

Next, we explored if this minimal A+B region could interact with IKKα. We performed RNA Immunoprecipitation (RIP) assays, where the RNA and protein are mixed *in vitro.* The IKKα

protein was immunoprecipitated by IKKα antibody or IgG (negative control) followed by RT-qPCR to detect the co-immunoprecipitation of the RNA with the protein (**Fig. 3A**). Consistent with previously published data, we observed FL DRAIC and RNA containing nts 705-950 of DRAIC displayed significant enrichment with IKKα [5]. However, further dissection of nts 705-950 showed that the 705-758 fragment, containing the prominent ABC hairpin associates with IKKα. Most interestingly, when A+B (the proximal part of the ABC hairpin) was deleted from 705-950, the ability to bind to IKKα was lost, while the A+B RNA alone could bind to IKKα (**Fig. 3B**). Therefore, the A+B part of the hairpin was necessary and sufficient for interaction with IKKα *in vitro*. Note that Luciferase and APTR RNAs were used as negative controls and did not co-precipitate with IKKα.

To visualize the protein-nucleic acid complex, we employed gel electrophoretic mobility shift assay (EMSA), where the mobility of the protein-nucleic acid complex is typically less than that of free nucleic acid [15, 16]. *In vitro* transcribed DRAIC RNA and IKKα protein were incubated at room temperature for 20-25 minutes in the presence of non-specific competitor tRNAs. We started with nts 705-777 RNA, which includes the A+B regions. After the reaction, the mixture was electrophoresed onto a 1.2% agarose gel and the RNA was visualized with SYBR Gold. As shown in **Fig. 3C**, compared to the no-protein-added lane (lane #1), a shifted band was observed in the presence of IKKα in an RNA dose-dependent manner (lane #6 & 7 & 8). However, no band was observed with GST protein alone (lane # 4), demonstrating that DRAIC physically interacts with IKKα. Notably no RNA contamination was observed in GST and IKKα proteins, as there were no signals detected in lane #3 and lane #4.

The specific interaction of A+B with IKKα was further confirmed by EMSA, where a shifted band was observed only in the presence of IKKα (lane #2), but not with GST-tagged NEMO (lane #3) or GST alone (lane #4) (**Fig. 3D**). The specificity of the interaction was validated by competition

experiments. Biotin-labeled A+B RNA probe was used in the EMSA in the presence of excess of unlabeled A+B RNA and tRNA, and the probe was visualized by transfer to membranes and HRP-conjugated streptavidin. A shifted band is seen (lane #2, red arrow), which was competed out by unlabeled A+B duplex in a dose-dependent manner (lane #3-7) (**Fig. 3E**). Concurrently, there was an increase in free biotin-labeled RNA running in the lower part of the membrane (blue arrow). The quantification of shifted to unshifted A+B RNA is shown at the bottom of the image. These results demonstrate that A+B specifically binds to IKKα.

A+B is necessary and sufficient for interaction with IKKα coiled-coil domain, but not IKKβ coiled-coil domain

Our published data showed that DRAIC moderately decreases the association of IKKα with NEMO [5]. Therefore, we wondered whether the inter-subunit interaction domain of the IKK subunits, specifically the coiled-coil domain, interacts with DRAIC.

We first tested if the IKKα coiled-coil domains (IKKα-ccd) bind to DRAIC. A RIP assay showed that both FL DRAIC and nts 705-950 of DRAIC were enriched in the immunoprecipitates of the MBP-IKKα-ccd when the protein was mixed with the RNA *in vitro* (**Fig. 4A**). However, no enrichment was observed with either of the negative control RNAs luciferase or APTR RNAs (**Fig. 4A**). We next tested whether hairpin A+B is necessary for DRAIC binding to the IKKα-ccd. The RIP assay showed that removing hairpin A+B from nts 705-950 abolished the enrichment of 705-950 DRAIC with MBP-IKKα-ccd. No RNA enrichment was observed with the MBP tag alone or with MBP-IKKα-ccd incubated with negative control RNAs, APTR, or luciferase (**Fig. 4B**). These results demonstrate that the binding of DRAIC to IKKα-ccd requires the presence of hairpin A+B.

Additionally, we produced MBP-IKKβ-ccd protein, containing the same number of amino acids as the IKKα-ccd, and carried out RIP after mixing RNA and protein in vitro. DRAIC 705-950 was

associated specifically with IKKα-ccd but not the IKKβ-ccd, (**Fig. 4C**). Interestingly, hairpin A+B displayed a high level of enrichment specifically with the MBP-IKKα-ccd, but not the MBP-IKKβ-ccd or MBP tag alone. These results demonstrate the specific binding of DRAIC 705-950 with IKKα-ccd, and that A+B hairpin alone is sufficient for this specific interaction.

A+B decreases the binding of NEMO coiled-coil to IKKα coiled-coil domain

The binding of the regulatory and substrate-interaction subunit NEMO of the IKK complex with kinase subunits IKKα or IKKβ is mediated by interactions between coiled-coil domains and is responsible for full substrate phosphorylation [9, 17]. We reported that DRAIC diminishes the interaction between IKKα and NEMO *in vitro* and *in vivo* [5]. Therefore, we investigated if the binding of hairpin A+B to the IKKα-ccd inhibits the binding of the NEMO-ccd to IKKα-ccd.

MBP-IKKα-ccd-Spot protein was immobilized on Spot beads and incubated with MBP-NEMO-ccd-His6 protein in the presence of FL DRAIC or negative control RNA, APTR. Pulling down the Spot-IKKα-ccd on Spot beads, followed by western blotting to detect NEMO-ccd-His6 using an anti-His tag measured the complex formation between the two ccd containing proteins. A significant decrease in NEMO-ccd pulled down by IKKα-ccd was observed in the presence of FL DRAIC RNA compared to APTR RNA (**Fig. 4D**, left). The hairpin A+B was then added instead of FL DRAIC, and this was sufficient to inhibit the interaction between the two IKK proteins (**Fig. 4E, F**). Therefore, the A+B RNA is sufficient to inhibit the interaction between the coiled-coil domains. In addition, the A+B RNA does not interact with the GST-NEMO (**Fig. 3D**) and so we believe that the inhibition is carried out through the interaction of the RNA with IKKα-ccd.

A+B binds to IKKα with high affinity and inhibits the phosphorylation of IκBα.

Surface Plasmon resonance [18, 19] was used to measure the affinity of IKKα with A+B RNA. His6 tagged IKKα was immobilized on the sensor chip by Ni^{2+}/NTA Beads and A+B RNA was

injected through the flow cell as the analyte. A dose-responsive binding was seen, and the calculated K_D of the interaction was 0.76 nM (**Fig. 5A**). When the reverse experiment was done with 5'biotin-tagged A+B bound to the sensor surface by NA chip as the ligand and IKKα injected as the analyte, we still saw dose responsive interaction, but the calculated K_D was 5.36 nM (**Fig. 5B**). The lower affinity when the RNA is tethered to the chip could be because of the absence of a spacer between the chip surface and the A+B RNA, leading to steric hindrance of the association with IKK protein [20]. Nevertheless, together the results suggest that the K_D of the interaction is in the range of 1-5 nM. SPR confirmed that A+B RNA does not interact with the NEMO **(Fig. 5C).**

A+B binds to IKKα and inhibits the phosphorylation of IκBα when expressed in cells.

We overexpressed DRAIC and various derivatives of DRAIC in HEK293T cells to test whether the A+B RNA is necessary and sufficient to interact with IKKα protein *in vivo*, consistent with what we observed *in vitro* in **Fig. 3**. Indeed, the A+B element is necessary (compare 705-950 with and without A+B) and sufficient (A+B) to interact with IKKα *in vivo* in RIP experiments (**Fig. 6A, B**).

Next, we tested which derivative of DRAIC can inhibit the kinase activity of IKK in cells. The cells were treated with the TNFα for 15 minutes to stimulate the phosphorylation of IκBα in the presence of MG132 to prevent the proteasomal degradation of the phosphorylated IκBα. Although the total level of IκBα did not change, the addition of TNFα stimulated its phosphorylation, and this phosphorylation was inhibited by FL DRAIC and 705-950 DRAIC **(Fig. 6C).** Deletion of A+B from 705-950 DRAIC (705-950 del. A+B) prevented the inhibition, while the A+B RNA alone was sufficient to inhibit the phosphorylation. Similar results were seen in four different cell lines suggesting the universality of these observations (**Fig. 6C, Supp. Fig.**

S1A and 1B). Thus, the A+B RNA is necessary and sufficient to inhibit the kinase activity of IKK *in vivo*, consistent with A+B being necessary and sufficient to physically associate with IKKα.

A+B inhibits cancer cell migration, invasion, and clonogenicity.

Finally, we investigated whether A+B affects tumor cell behavior similarly to FL DRAIC. We transfected various DRAIC fragments (FL, 705-950, 705-950 del. A+B, A+B only, and 900-1705) into several cancer cell lines (HeLa, PC3M, and C4-2B) and measured the impact of A+B on tumor cell behavior. RT-qPCR confirmed the successful overexpression of different DRAIC fragments in cells (**Supp. Fig. S2, Fig. S3B and S3D**).

In the Matrigel Invasion Assay, the tumor cells are seeded in a chamber containing a Matrigel extracellular matrix and asked to invade through the matrix to the bottom surface of the membrane[21]. The images of the cells and the quantitation of the results are shown (**Fig. 6D-E and Supp. Fig. S3Aand S3C**). Consistent with our previously published data, FL and 705-950 DRAIC significantly inhibited tumor cell invasion[5]. The A+B DRAIC fragment also significantly decreased tumor cell invasion; however, removing A+B from 705-950 completely abolished this effect, demonstrating that A+B is required for DRAIC to inhibit tumor cell invasion (**Fig. 6D and Supp. Fig. S3Aand S3C**). This inhibition was observed in three different cell lines.

Next, we tested if A+B affects tumor cell migration by performing a wound-healing assay[22]. As displayed in **Fig. 6F** and quantitated in **6G**, the gap ("wound") was almost closed in both EV and 900-1705 DRAIC, while significant gaps remained in FL, 705-950, and A+B DRAIC. Removing A+B from 705-950 nullified the inhibition of migration by 705-950.

Lastly, we tested if A+B influences the clonogenic cell growth in culture. Tumor cells were seeded on tissue culture plates, and we observed that FL, 705-950, and A+B significantly decreased the number of colonies compared to EV and 900-1705 DRAIC **(Fig. 6H).** However,

removing A+B from 705-950 abolished this inhibition. Taken together, the A+B part of DRAIC is necessary and sufficient to inhibit tumor cell invasion, migration, and clonogenic growth.

A+B is contained in an alternative exon 4a, whose inclusion or exclusion differs between cell lines.

An examination of RNAseq data from cell lines revealed an alternative splicing event with an alternate splice acceptor site that extends the constitutive exon 4 by adding a 5' extension, exon 4a (**Fig. 7A**). Interesting, exon 4a encodes the bottom strand of the A+B+C hairpin (**Fig. 1**).

To evaluate the clinical significance of the A+B containing transcript exon 3-4a-4, we analyzed its expression across multiple cell lines. Sashimi plots showed the exon 3-4a-4 DRAIC isoform was predominantly expressed in LNCaP and LUAD NCI-H2801 cells, while PC3 and DU145 cells mainly expressed isoforms lacking exon 4a (designated as exon 3-4 isoforms). RT-PCR confirmed the differential expression of isoforms with and without exon 4a in several cell lines (**Fig. 7B**). Notably no genomic DNA contamination was observed in the cDNA, as there was no signal detected in the RNA samples without RT **(Fig. 7B** the middle panel). RNA-Seq analysis demonstrated reduced expression of NF-κB regulated inflammatory genes in LNCaP (with exon 4a) compared to DU145 (without exon 4a) (**Fig. 7C**).

Tumors expressing exon 4a have lower expression of NF-κB target genes

We next turned to tumors showing differential expression of the exon 4a containing isoform. Lung adenocarcinomas (LUAD) were the only tumor type with sufficient tumors expressing either splice junction exon 3-4a-4 or exon 3-4. GSEA was conducted after stratifying tumors based on expression of the exon 3-4a junction or the 3-4 junction. The results show that tumors with lower expression of exon 4a had higher activity of NF-κB driven genes compared to tumors

with high expression of exon 4a (**Fig. 7D**), while this difference was not seen when the tumors were stratified by expression of exon 4 (**Fig. 7E**).

To extend this result, we identified LUADs that exclusively express exon 3-4a junction (with no exon 3-4 junction) (**Subset A in Table 1A**) and vice versa. Only 8 tumors completely skipped exon 4a (**Subset B in Table 1A**) and we selected 8 matching tumors that included exon 4a from Subset A. The tumors were matched by the level of expression of the total DRAIC transcript (**Table 1B**) to eliminate any complications from differential expression of all DRAIC isoforms. Heatmap of NF-κB target genes confirms that although the matched tumors express equal levels of all DRAIC isoforms, expression of exon 4a (Subset A) is associated with decreased NF-κB target gene expression (**Fig. 7F**).

Discussion

Identification and Specificity of the A+B RNA Structure We utilized SHAPE-MaP to model the secondary structure of a key functional region of DRAIC. The DRAIC lncRNA regulates the NF-κB signaling pathway by interacting with the two subunits of the IKK complex. Our findings identified a critical 36-nucleotide hairpin within DRAIC, plays a key role in modulating NF-κB activity, as it is both necessary and sufficient for inhibiting NF-κB signaling by interacting specifically with IKKα. Other studies [23] have identified broad functional or protein binding regions within lncRNAs, generally spanning over 200 nucleotides in length, making discovery of this 36nt A+B hairpin - comparable in size to microRNAs - remarkable. This compact, highly functional region highlights the potential therapeutic significance of identifying minimal structural elements of the RNA for therapeutic purposes. Future studies should focus on determining whether the functionality of this hairpin arises from specific nucleotide interactions or the structural integrity of the hairpin. Notably, other hairpins predicted by SHAPE-MaP at the 3' end

of DRAIC did not exhibit inhibitory activity, indicating the unique specificity of the A+B structure in NF-κB inhibition.

The interaction of A+B with a specific subunit of IKK. The physical interaction between the A+B hairpin and IKKα, but not NEMO or IKKβ, again supports the specificity of this RNA-protein interaction. This specificity is further corroborated by our findings that A+B directly interacts with the coiled-coil domain of IKKα, a region known to be crucial for the assembly and activation of the IKK complex [9, 24]. Coiled-coil domains, characterized by their intertwined α-helices, are notoriously difficult to disrupt due to their stable hydrophobic core and specific interhelical interactions [25]. These features make the coiled-coil domain of IKKα an especially challenging target for therapeutic intervention. Despite this stability, A+B could efficiently disrupt the binding of NEMO-coiled coil domain to IKKα-coiled coil domains, offering a promising avenue for therapeutic intervention in a wide range of diseases driven by the NF- κB pathway. Many cancers exhibit constitutive activation of the NF-κB pathway, leading to uncontrolled cell proliferation, resistance to apoptosis, and enhanced metastatic potential [26]. By inhibiting the NEMO-IKKα interaction, A+B could reduce NF-κB-mediated transcription of oncogenes and survival factors, making it a potential therapeutic agent in cancers where NF-κB plays a pivotal role. Additionally, A+B could enhance the sensitivity of cancer cells to chemotherapy or radiation therapy by lowering their resistance mechanisms mediated through NF-κB. Clearly, detailed mechanistic studies to understand how A+B disrupts the NEMO-IKKα interaction at the molecular level such as by X-Ray Crystallography is needed.

The inability of A+B to bind to the coiled-coil domain of IKKβ (**Fig. 4C**) is supportive of our previous observation that FL DRAIC RNA bound more much better to IKKα than to IKKβ *in vitro*, and disrupted the association of IKKα with NEMO, but not that of IKKβ with NEMO [5]. This selectivity for the α subunit over the β subunit, both of which are catalytic, and both of which

could homodimerize with NEMO to form a functional IKK, suggests that one way cancer cells may escape the inhibition of IKK and NF-κB is by expressing more IKKβ than IKKα [27, 28] or in rare cases, by activating NF-κB independent of IKKα [29]. This model could be a potential explanation for why there are some cancers where DRAIC is not tumor suppressive, e.g. breast cancer [30].

NEMO plays a pivotal role in the canonical NF-κB signaling pathway, acting as a regulatory subunit of the IKK complex. The binding of NEMO to IKKα and IKKβ is required for the kinase activation, thus leading to the phosphorylation and activation of NF-κB [31]. In addition, it is also reported that NEMO inhibits the receptor interacting with protein-1 (RIP1) from activating CASPASE-8, thereby preventing apoptosis independent of the NF-κB signaling pathway [32, 33]. Targeting NEMO and NF-κB signaling pathway is a promising strategy for cancer treatment. Our study demonstrates that FL DRAIC and DRAIC 701-905 also interacted with NEMO [5], suggesting that DRAIC can modulate the NF-κB pathway by interfering with NEMO's function. However, it is noteworthy that the A+B regions of DRAIC did not associate with NEMO (**Fig. 3D and 5C**), implying that there are adjoining parts of the RNA, contained in 701-905, but not A+B, which interact with NEMO. Identifying and characterizing these interaction sites could provide deeper insights into the mechanism by which DRAIC inhibits IKK activation.

Affinity of interaction and mechanism of interaction. Surface plasmon resonance (SPR) has been widely utilized to study the binding affinity of proteins, peptides, and small molecules [18], but its application to the study of lncRNAs and their interactions with proteins is still relatively novel. In the current study, we used this technology to study the interaction of A+B DRAIC lncRNA and IKKα. We observed binding affinities in the low nanomolar range (< 6nM) using different ligand immobilization methods, and no binding was detected with GST-NEMO, suggesting that the interaction is specific to IKKα and the A+B RNA itself. The fast association

(higher K_a) and slow disassociation (lower K_d) suggest that DRAIC can quickly engage with IKKα and remain bound long enough to effectively disrupt the interaction between IKKα and NEMO, leading to sustained inhibition of NF-κB signaling. The unexpectedly high affinity of the A+B hairpin's interaction with IKKα is intriguing and suggests that DRAIC (or its A+B regions) strongly and specifically interacts with IKKα, potentially making it an effective inhibitor of IKKα's role in the NF-κB pathway, and further structural studies are necessary to determine whether this affinity is solely due to interactions with the coiled-coil domain or if other regions of IKKα are also involved. The nanomolar K_D for A+B binding to IKKα is comparable to other RNA-protein interactions. For example, Nelson et al. reported a binding affinity of 14 nM for the interaction between MHV N protein and RNA [34], while Chen et al. determined a K_D of 2.82 nM for the binding of IBV N protein to the IBV leader [35]. The slight discrepancy between the two K_D values in our experiments may be attributed to: (i) the method of ligand immobilization, which could result in improper orientation and reduced accessibility of the binding site, and (ii) the differing surface chemistries of the NTA and NA chips, which may influence their interaction with analytes [36]. RNA-protein interactions can be mediated by the RNA backbone, where the secondary structure plays a critical role, or by specific interactions between nucleotides and amino acids, making the RNA sequence important for complex formation. Future experiments will therefore explore whether the hairpin structure of A+B or specific sequences within A+B are crucial for its high-affinity interaction with IKKα.

Short RNA as a disruptor of coiled-coil domain interactions. To the best of our knowledge, this is the first instance of a short RNA interacting with such high affinity with a coiled-coil domain and disrupting the interaction of two coiled-coil domains. As has been mentioned above, dimerization mediated by coiled-coil domains is wide-spread in biology and there have been repeated attempts to discover agents that can disrupt such interaction for therapeutic

purpose. Thus, we are excited by the possibility that short RNAs, like A+B, can be designed that will selectively disrupt many other coiled-coil domain interactions for therapy.

Alternative splicing modulates the activity of DRAIC. To the best of our knowledge this is the first example where alternative splicing of a lncRNA removes a critical functional module of the RNA. The results from the cancer cell lines and the lung adenocarcinomas in TCGA suggest that the inclusion of Exon 4a, which constitutes half of the A+B hairpin, is associated with repression of NF-κB, as is expected from our prior biochemical and cell biological results. An interesting possibility is that physiological or pathological regulation of this alternative splicing event will activate or inactivate a regulator of NF-κB signaling. The results also imply that when assessing the role of some lncRNAs in tumor progression, it is important to assess which splice isoform is expressed, and that some contradictory effects ascribed to a lncRNA in the Literature could stem from different splice-isoforms being expressed. However, LncRNAs often have many splice isoforms, making it difficult to assess which isoforms should be studied separately. Thus, it is important to do structure-function analyses as done here to determine which functional modules are likely to be regulated by alternative splicing and then separately studying the functionally different isoforms of the lncRNA.

Inhibition of IKK and Therapeutic Application. The phosphorylation and subsequent degradation of IκBα is a crucial step in the activation of NF-κB, allowing the transcription factor to translocate from the cytoplasm to the nucleus and initiate gene expression [33, 37]. In our study, we found that the A+B hairpin effectively inhibits the phosphorylation of IκBα in cells, thereby blocking a key step in the canonical NF-κB activation pathway. This inhibition likely contributes to the observed decrease in NF-κB activity in cells with high DRAIC expression. If this inhibitory effect can be replicated in vitro using soluble IKK, it would enable us to elucidate the precise mechanism of action—whether the interaction with the coiled-coil domain and the

disruption of the IKKα complex is the primary or sole means by which A+B exerts its kinase inhibition.

Given the ability of the A+B hairpin within DRAIC to suppress cancer cell migration, invasion, and clonogenicity, its biological significance is clear. These findings indicate that the A+B hairpin not only plays a crucial role in modulating NF-κB signaling but also serves as a potent inhibitor of aggressive cancer phenotypes. This dual function highlights the therapeutic potential of targeting the A+B hairpin structure in cancers characterized by hyperactive NF-κB signaling. A therapeutic strategy centered on the A+B hairpin could involve designing small molecules, antisense oligonucleotides, or RNA mimics that specifically stabilize or enhance the hairpin's interaction with IKKα. By doing so, this approach could inhibit NF-κB activation and consequently reduce tumor progression, invasion, and metastasis. Additionally, given the specificity of the A+B hairpin for IKKα over IKKβ and NEMO, targeting this hairpin could provide a more precise therapeutic approach with fewer off-target effects, particularly in cancers where IKKα driven NF-κB signaling is a driving factor.

Moreover, combining this strategy with other therapies that target different components of the NF-κB pathway or other oncogenic pathways could enhance the overall efficacy of cancer treatment, potentially overcoming resistance mechanisms that are common in aggressive cancers. Therefore, the A+B hairpin within DRAIC represents a promising therapeutic target, offering new avenues for the development of cancer treatments aimed at curbing the malignancy associated with hyperactive NF-κB signaling.

In conclusion, our study identifies a critical secondary structure within DRAIC that specifically interacts with IKKα to inhibit NF-κB signaling and suppress cancer cell aggressiveness. The specificity of the A+B hairpin in binding to IKKα, coupled with its functional effects on NF-κB signaling and cancer cell behavior, highlights the potential of targeting this RNA structure for

therapeutic intervention in NF-κB driven cancers. Identifying the A+B functional module also allowed us to identify functionally different isoforms of DRAIC generated by alternative splicing. Future studies should explore the detailed molecular mechanisms by which the A+B hairpin modulates IKKα activity and the broader implications of these findings for cancer therapy.

Material and Methods

Cell culture and transfection

Prostate cancer cell lines LNCaP, C4-2B, DU145, PC3, T47D, U373 and PC3M were cultured in RPMI 1640 medium supplemented with 10% FBS, 1% penicillin/streptomycin, 1 mmol/L sodium pyruvate, and 10 mmol/L HEPES buffer. HeLa and HEK293T cells were cultured in DMEM medium supplemented with 10% FBS and 1% penicillin/streptomycin. All the cells were maintained in a humidified cell culture incubator at 37°C in the presence of 5% CO_2. For NF-κB luciferase reporter assays, cells were co-transfected with NF-κB firefly luciferase reporter plasmid, Renilla luciferase plasmid, and DRAIC fragments using Lipofectamine 3000 (Life Technology, cat. no. 3000001) following the manufacturer's instructions. Twenty-four hours post-transfection, cells were washed and lysed in 1x passive lysis buffer (Dual-Luciferase Reporter Assay, Promega, cat. no. E1980), and luminescence signals were captured by GloMax 96 microplate luminometer (Promega, cat.no. E6521). For overexpression of different portions of DRAIC in cells, DRAIC fragments were first cloned into a pcDNA3 backbone as previously described[5]. After sequence confirmation of the plasmids, DRAIC fragments were transfected into cells using Lipofectamine 3000.

Quantitative Reverse Transcription PCR (RT-qPCR) and Western Blotting

To confirm the successful overexpression of DRAIC fragments in cells after transfection, total RNA was extracted using Direct-zol RNA Miniprep kit (ZYMO Research, cat. no. R2052). cDNA

was synthesized from equal amount of RNA by using the PrimeScript RT Reagent kit (Takara, cat. no. RR037). RT-qPCR was performed using an ABI Prism 7500 fast system (Applied Biosystems) with the 2x qPCR Master Mix (NEB, cat. no. M3003). For each gene, the relative expression levels were normalized to glyceraldehyde 3-phosphate dehydrogenase (GAPDH). All experiments were conducted at least 2-3 times in triplicate, with results presented as mean values ± S.E.M. PCR was conducted with primers designed to flank exon 3 and exon 4 to detect isoforms either containing or lacking exon 4a. The reaction was carried out for a total of 28 cycles. All primer information is listed in **Table S1**.

Phosphorylation of IκBα

For detecting the level of p-IκBα, an equal number of cells was plated in 6-well plate for overnight. The next day, cells were pretreated with MG132 for 2 hours and then treated with TNFα (20ng/ml) for 15 minutes. After 15 minutes, cells were washed with cold PBS, then 300ul 2XSDS sample buffer (containing 5% β-ME) was added to lyse the cells. Lysates were loaded onto 12% SDS-PAGE gel for protein separation and immunoblotted with anti-phosphor IκBα antibody (Abcam, cat.no. ab133462, 1:4000 dilution). The membrane was transferred by Semi-dry transfer system (Bio-Rad) and followed by Ponceau S staining to see the overall protein loading in each group. The total levels of IκBα was also probed as loading controls using anti-IκBα (CST, cat. No.9242). All gel images were obtained on ChemiDoc™ touch system with Image Lab Touch software (Bio-Rad).

Clonogenic Assay, Wound Healing Assay, and Matrigel Invasion Assay

To evaluate the ability of a single cell to form a colony, a plastic clonogenic assay was conducted. DRAIC fragment-containing cells were diluted to 500 cells/ml and seeded into a 6-well plate, then continuously cultured for 9 days (with fresh media replaced 5 days after seeding). Colonies were fixed with glutaraldehyde (5.0% v/v), stained with crystal violet (0.5%

w/v), and images were acquired by ChemiDoc™, the number of colonies in each well were counted.

To evaluate cell migration, cells were seeded on a 24-well plate at 2.5 x 10^5/well overnight. The next day, after cells reached 100% confluency, wounds were generated using a 10 μL micropipette tip. Floating cells were removed and washed with PBS three times, and complete cell culture media were added to each well. Images (3-5 random fields/well, quadruplicate per group) were captured immediately after media replacement (T = 0) and 20 hours (T = 20) after wound generation at 10× magnification (Leica Microscope). After exporting images, wound areas were measured using ImageJ (NIH). Briefly, the polygon selection tool was used to indicate the wound area, and the areas were quantified (Analysis > Measure). The extent of closure at T20 was calculated by subtracting the area at T0, and the percentage closure was determined by normalizing the difference to the area at T0 [22, 38].

To evaluate cell invasion, the Matrigel-containing Boyden chamber (Corning, cat.no. 354480) was first rehydrated with serum-free medium at 37°C for 2 hours before seeding the cells. Cells were starved overnight, and then a total of 1 x 10^5 cells were seeded in serum-free medium in the top of the chamber. The bottom of the chamber contained full growth medium (10% FBS) as a chemoattractant, and the chamber was incubated at 37°C in the presence of 5% CO_2. After 19-20 hours, the chambers were gently washed with 1x PBS. The non-invading cells from the upper surface of the chamber were gently removed using Kimwipes or cotton swabs. The invaded cells were treated with 4% PFA for 10 minutes, followed by 0.5% crystal violet staining at room temperature for 15-30 minutes to visualize. The invaded cells were captured under a microscope (Leica or KENYEN) as detailed in the Figure legends.

RNA immunoprecipitation (RIP), RNA pull-down, Co-Immunoprecipitation (Co-IP) assay.

The full-length DRAIC (FL), 705-950, 705-950 del. A+B, 900-1705, and other fragments of DRAIC were prepared by PCR (primers provided in **Table S1**) and used as templates for *in vitro* transcription (IVT) reaction by the T7 promoter using T7 polymerase and the HiScribe T7 High Yield RNA Synthesis kit (NEB, cat. no. E2040L). Template DNAs were removed by treating with DNase I at 37°C for 30 minutes and the IVT RNAs were further purified by RNA purification kit (NEB, cat. no. T2040L). The size of each IVT RNA was also confirmed by agarose gel electrophoresis. To elucidate the binding portion of DRAIC on IKKα (Life Technology cat. no. PR7619B), an RNA pull-down assay was performed as previously described[5]. Briefly, IVT DRAIC RNAs (1 μg/reaction) were heated at 95°C for 2 minutes, chilled on ice for 2 minutes, and then slowly cooled to RT for 15 minutes in RNA folding buffer. Refolded RNA was incubated with His-IKKα (100 ng/reaction) at RT for 1 hour in RNA binding buffer (25 mM HEPES, pH 7.5, 150 mM NaCl, 0.05% NP-40, 10% glycerol, protease, and RNase inhibitors) and RNA-IKKα complex was pulled down by Ni^{2+}-NTA Agarose Beads (Qiagen cat. no. 30230) or IKKα antibody. The unbounded RNA was removed by wash buffer. RNA was extracted from the complex using TRIzol RNA isolation reagent (Life Technology, cat. no. 15596260). cDNA was synthesized and RT-qPCR was performed to see if DRAIC RNA was enriched in IKKα or not.

To check if A+B DRAIC was interacting with IKKα in cells, 293T cells expressing different portions of DRAIC were lysed in PEB (polysome extraction buffer: 20 mM Tris-HCl pH 7.5, 100 mM KCl, 5 mM MgCl2, 0.5% NP-50) cell lysis buffer freshly supplemented with protease and RNase inhibitors. An equal amount of protein (0.5 mg/reaction) was first pre-cleared with protein A/G agarose beads (Santa Cruz, cat. no. sc2003), followed by incubation with anti-IKKα antibody (CST, cat. no. 2682S, 1:200 dilution) and IgG as a negative control at 4°C overnight. The next day, protein A/G agarose beads were added to each tube to immunoprecipitate the related protein. After five washes with NT2 buffer (20 mM Tris-HCl pH 7.4, 150 mM NaCl, 1 mM $MgCl_2$, 0.05% NP-40) with protease and RNase inhibitors (NEB, cat. no. M0314S), half of each

sample was directly added with 2x SDS sample buffer for immunoblotting with anti-IKKα antibody. The other half of each sample was used to extract RNA using TRIzol reagent following the manufacturer's instructions. cDNA was synthesized and RT-qPCR was performed using DRAIC-specific primers to see if DRAIC RNA was enriched to IKKα or not.

In vitro IKK complex formation assay

To evaluate if FL and A+B DRAIC RNA will interfere with the binding of NEMO to IKKα, we conducted the IKK complex formation assay. Briefly, Spot-tagged IKKα coiled-coil domain protein was immobilized on Spot-Trap magnetic beads (Proteintech cat. no. ETDMA). His-tagged NEMO coiled-coil domain and either FL DRAIC or A+B RNA was added and incubated for 2 hours at 4°C. The NEMO associated with IKKα was then pulled down by magnetic beads, and after five washes with NT2 buffer, 2x SDS sample buffer (β-ME freshly added) was added to the complex. The presence of IKKα coiled-coil protein and NEMO coiled-coil protein was detected using anti-Spot antibody (Proteintech cat. no. 26A5, 1:4000 dilution) and anti-His tag antibody (Qiagen, cat. no. 34650, 1:4000 dilution), respectively.

Cell-free SHAPE-MaP

The general strategy has been described previously [39]. LNCaP cells grew to 80% confluency in two 15-cm dishes. Both plates were washed once in PBS before scraping and lysis in 2.5 mL of proteinase K buffer (40 mM Tris, pH 8, 200 mM NaCl, 1.5% sodium dodecyl sulfate, and 0.5 mg/mL proteinase K). Proteins were digested for 45 min at 23 °C with intermittent mixing. Nucleic acids were extracted twice with one volume of phenol: chloroform:isoamyl alcohol (25:24:1) that was pre-equilibrated with 1.1x RNA folding buffer (110 mM HEPES, pH 8, 110 mM NaCl, 5.5 mM MgCl2). Excess phenol was removed through two extractions with one volume of chloroform. The final aqueous layer was exchanged into 1.1x RNA folding buffer using PD-10 desalting columns (GE Healthcare Life Sciences). The resulting RNA solution was incubated at

37 °C for 20 minutes before being split into two equal volumes. The SHAPE reagent, 5-nitroisatoic anhydride (5NIA, AstaTech) in DMSO was added to a final concentration of 62.5mM to one aliquot, and DMSO added to the other. Samples were incubated at 37 °C for 10 minutes. RNA was precipitated with 1/10 volume of 2 M ammonuim acetate and one volume of isopropanol. After washing with 75% (v/v) ethanol, the resulting pellet was dried and resuspended in 88 mL water. 10 mL of 10x TURBO DNase buffer and four units of TURBO DNase (Thermo Fisher) were added and, the mixture was incubated at 37 °C for 1h. RNA was purified (GeneJET RNA Cleanup and Concentration Micro Kit, Fisher) and eluted into 20 mL of nuclease-free water. 1µg of each RNA sample was subjected to MaP reverse transcription (MaP-RT) [20] using a DRAIC-specific primer (**Table S1**). For second-strand cDNA synthesis, the output DNA was used as a template for PCR with primers made to amplify a region of DRAIC containing the functional fragment, with the product including nt 655-1132. Purified PCR products were measured (Qubit dsDNA HS Assay Kit), and 2 ng were used as a template for 10 additional cycles of PCR to add Illumina-specific sequences and sample barcodes. Size distributions and purities of *DRAIC* amplicon libraries were verified (2100 Bioanalyzer, Agilent). Libraries (about 120 amol of each) were sequenced on a MiSeq instrument (Illumina) using a 250x250 paired end sequencing kit. ShapeMapper2 software was used to counts mutations and generate SHAPE profiles [40], and the SuperFold [41] was used with experimental SHAPE data to inform RNA structure modeling. Secondary structure projection images were generated using VARNA [42].

Electrophoretic Mobility Shift Assay (EMSA)

To visualize the protein-nucleotide complex, we conducted a gel electrophoretic mobility shift assay (EMSA) using the LightShift™ Chemiluminescent RNA EMSA Kit (Life Technology, cat. no. 20158) according to the manufacturer's instructions. Briefly, the in vitro transcribed unlabeled 705-777 DRAIC and A+B DRAIC RNA was incubated with IKKα-His or GST-NEMO

protein for 25 minutes at room temperature. After 25 minutes, 6x loading dye was added to the reaction mixture, which was then loaded onto a 1.2% agarose gel in 0.5x TB buffer (45 mM Tris, 45 mM boric acid) and run at 90-100 volts for 45 minutes. After electrophoresis, gels were stained for 20 minutes with 2× SYBR Gold (Invitrogen) while shaking. To reduce background signal, the agarose gel was destained in ~150 mL 0.5× TB for 15 minutes with shaking[15].

Competitive EMSA was performed using biotin-labeled A+B DRAIC RNA (produced by Gene Scripts) in the presence of excess unlabeled A+B DRAIC RNA (homemade). The reaction mixture was loaded onto a 6% DNA retardation gel (Life Technology, cat. no. EC6365BOX) in 0.25X TBE buffer and run at 90-100 volts for 45 minutes. After electrophoresis, the binding reaction was transferred to a positively charged nylon membrane (Life Technology, cat.no. AM10100) by wet transfer in 0.25X TBE buffer at 300 mA on ice for 50 minutes. The membrane was removed from the transfer system and cross-linked at 120 mJ/cm² using a commercial UV-light crosslinker. The membrane was then blocked with the Nucleic Acid Detection Blocking Buffer at room temperature for 15 minutes with gentle shaking. After blocking, the membrane was incubated with the conjugate/blocking solution (1:300 dilution) at room temperature for 15 minutes with gentle shaking. Following 4-5 washes with 1x wash buffer, the membrane was developed using X-ray film or ChemiDoc Image developer with enhanced ECL.

Surface Plasmon Resonance (SPR)

Surface Plasmon Resonance (SPR) experiments were performed using a Biacore T200 (GE Healthcare) at 25 °C, with HBS-EP serving as the running buffer (0.01 M HEPES, pH 7.4, 0.15 M NaCl, 3 mM EDTA, 0.05% vol/vol Surfactant P20 [GE]). An NTA (nitrilotriacetic acid) chip (Cytiva, cat. No. BR100407), used to immobilize the IKKα-His protein, was activated by injecting a 0.5 mM $NiCl_2$ solution in the running buffer. The IKKα-His protein, at a concentration of 20 ng/μL in running buffer, was injected at a flow rate of 10 μL/min with a contact time of 60

seconds. The 5' Biotin A+B RNA was similarly diluted in running buffer prior to injection. To ensure stable responses, three start-up cycles were performed over both the control and active surfaces before the analysis started. For regeneration, a solution of running buffer containing 0.35 M EDTA was employed to remove the nickel and any chelated molecules from the chip surface. For the inverse analysis, the 5' Biotin A+B RNA was captured on an NA (NeutrAvidin) chip (Cytiva, cat. No. 29407997) following the manufacture instructions and [43], and varying doses of IKKα-His protein, diluted in the running buffer, were injected over the captured RNA. Sensorgrams were globally fit to 1:1 binding model using Biacore T-200 evaluation software version 1.0[44].

Purification of full-length recombinant NEMO, IKKα protein and the coiled-coil domains of IKK complex

The purification of GST-NEMO was performed as previously[45]. In brief, the pGEX-NEMO plasmid was transformed into Rosetta BL21 cells, which were cultured in LB medium containing 100 μg/ml ampicillin. NEMO protein expression was induced by adding 0.3 mM IPTG at 28°C for 3 hours, and the protein was purified using glutathione agarose beads.

For the purification of full-length IKKα protein, the IKKα cDNA was first subcloned into the pMAL-c5X vector using mutagenesis. After sequence confirmation of the correct clone, the pMAL-c5X-IKKα-6His construct was transformed into Shuffle T7 competent E. coli cells (NEB, cat. No.C3026J), and the cells were cultured in LB medium with 100 μg/ml ampicillin. Protein expression was induced with 0.1 mM IPTG at 28°C overnight. IKKα protein was purified from inclusion bodies. Cells were harvested by centrifugation at 4000 RPM for 20 minutes at 4°C and lysed in 2X PBS supplemented with 1 mM DTT, 10% glycerol, and 0.1% NP-40, followed by sonication. The lysate was then centrifuged at 10,000 g for 15 minutes to remove the supernatant. The pellet was resuspended in 2X PBS containing 10% glycerol, 0.5 mM DTT, and

1% (w/v) sarkosyl, and incubated at room temperature on a rocker at 120 rpm for 16 hours, followed by sonication. The supernatant was collected and dialyzed against 2 liters of dialysis buffer (2X PBS with 0.2 mM DTT and 15 mM imidazole) to remove sarkosyl, with buffer changes twice overnight at room temperature. After dialysis, the supernatant was subjected to nickel affinity purification as previously described[46]. The coiled-coil domain of IKK were also subcloned into the MBP tagged plasmid backbone with different tags, respectively. And the coiled-coil domain proteins were purified by using the same method, specific to each tag.

Bioinformatics analysis

Raw RNA-Seq files for prostate and lung cancer cell lines from the Cancer Cell Line Encyclopedia (CCLE) database were downloaded from the NCBI Bioproject PRJNA523380 [47, 48]using the prefetch tool (https://github.com/ncbi/sra-tools) and converted to FASTQ format using fasterq-dump. Quality control was performed by using the BBduk from the BBTools package (https://doi.org:https://jgi.doe.gov/data-and-tools/software-tools/bbtools/bb-tools-user-guide/) to remove adapters, and trim bases below 20 and discard reads shorter. The GRCh38 reference genome was indexed using hisat2-build[49] and aligned to reference genome using hisat2. SAM files were converted to BAM format, sorted and indexed using samtools for downstream analyses [50].

The controlled RNA-Seq BAM files for the lung adenocarcinoma from the TCGA (TCGA-LUAD) were downloaded from the Database of Genotypes and Phenotypes (dbGAP) using the gdc-client tool.

To detect DRAIC isoforms (exon 3-4a-4 and exon 3-4), specific 40-base probes were designed. For exon 3-4a-4, the probe included the last 5 bases of exon 3, 30 bases from exon 4a, and the first 5 bases of exon 4. For exon 3-4, the probe comprised the last 20 bases of exon 3 and the first 20 bases of exon 4 (sequences in Supp. Table 2). Probes were mapped to RNA-Seq reads,

and isoform-specific expression was quantified as counts per million (CPM = (Raw Counts/Total Mapped Reads) × 10^6). The scaling factor 10^6 is the normalizing factor for variations in sequencing depth between samples.

Normalized RNA-Seq data (DESeq2) from TCGA-LUAD were stratified by isoform expression into low (Q1) and high (Q4) groups for exon 3-4a-4 and exon 3-4. Differential expression between groups was analyzed using GSEA v4.3.3 [50]. We used the MSigDB gene set collection, including the BIOCARTA_NFKB_PATHWAY, GOBP_NON_CANONICAL_NF_KAPPAB_SIGNAL_TRANSDUCTION, and HALLMARK_TNFA_SIGNALING_VIA_NFKB gene sets. Parameters included a maximum gene set size of 5000, minimum size of 10, 1000 permutations, and weighted enrichment statistics.

DU145 (GSM618472-GSM618477) and LNCaP (GSM618479-GSM618485) BAM files were downloaded from GEO (GSE25183) and processed according to the submitter's instructions. Differentially expressed genes (DEGs) were visualized using the R package Pheatmap.

Statistical analysis

All data are presented as mean ± SEM. Statistical analyses were conducted using GraphPad Prism (version 8.0.2, GraphPad Software Inc., San Diego, CA). Comparisons between two groups were performed using one-tailed, unpaired Student's *t*-tests. For comparisons involving more than two groups, one-way or two-way ANOVA followed by Tukey's post-hoc test was applied. A *p* value of less than 0.05 was considered statistically significant.

Data Availability Statement

The original contributions of this study are available in the article and Supplementary Material. The SHAPE-MaP libraries data files have been deposited in the Gene Expression Omnibus

(GEO) database under accession number GSE279192. For further inquiries, please contact the corresponding author.

Conflict of interest

K.M.W is a founder of ForagR Medicines, A-Form Solutions and Ribometrix. The other authors declare that there is no conflict of interest.

Acknowledgment

We express our gratitude to members of the Dutta laboratory (particularly Etsuko Shibata and Yoshiyuki Shibata). Special thanks to Dr. Edlue M. Tawengwa for assistance in the SPR experiment. The figures are formatted in Biorender.com. This work was supported by grants from the NIH (R01 GM146756 to A.D., and R35 GM122532 to K.M.W.), an American Cancer Society Postdoctoral Fellowship (ACS 130845-RSG-17-114-01-RMC to C.A.W.), a Predoctoral Fellowship from the American Heart Association (18PRE33990261 to R.K.P.), Wagner fellowships from the University of Virginia (to R.K.P.) and the F99/K00 NCI Predoctoral to Postdoctoral Fellow Transition Award (F99/K00CA253732 to R.K.P.). UAB Multidisciplinary Molecular Interaction Core (MMIC) is funded by NIH award 1S10RR026935

Author Contributions

XH, RKP and YC designed the experiments, DS performed the bioinformatics analyses and CW performed the SHAPE-Map analysis. XH, RKP, YC, CW and IN performed the experiments and analyzed the data. AD and KMW supervised the study. AD and XH wrote the manuscript, and all authors reviewed and approved the final version of the manuscript.

Reference

1. Qian, Y., L. Shi, and Z. Luo, *Long Non-coding RNAs in Cancer: Implications for Diagnosis, Prognosis, and Therapy.* Front Med (Lausanne), 2020. **7**: p. 612393.

2. Quinn, J.J. and H.Y. Chang, *Unique features of long non-coding RNA biogenesis and function.* Nat Rev Genet, 2016. **17**(1): p. 47-62.
3. Vance, K.W. and C.P. Ponting, *Transcriptional regulatory functions of nuclear long noncoding RNAs.* Trends Genet, 2014. **30**(8): p. 348-55.
4. Statello, L., et al., *Gene regulation by long non-coding RNAs and its biological functions.* Nat Rev Mol Cell Biol, 2021. **22**(2): p. 96-118.
5. Saha, S., et al., *Long Noncoding RNA DRAIC Inhibits Prostate Cancer Progression by Interacting with IKK to Inhibit NF-kappaB Activation.* Cancer Res, 2020. **80**(5): p. 950-963.
6. Sakurai, K., et al., *The lncRNA DRAIC/PCAT29 Locus Constitutes a Tumor-Suppressive Nexus.* Mol Cancer Res, 2015. **13**(5): p. 828-38.
7. Yao, Q., X. Zhang, and D. Chen, *The emerging potentials of lncRNA DRAIC in human cancers.* Front Oncol, 2022. **12**: p. 867670.
8. Saha, S., et al., *The tumor-suppressive long noncoding RNA DRAIC inhibits protein translation and induces autophagy by activating AMPK.* J Cell Sci, 2021. **134**(24).
9. Israel, A., *The IKK complex, a central regulator of NF-kappaB activation.* Cold Spring Harb Perspect Biol, 2010. **2**(3): p. a000158.
10. Zhang, Z., et al., *LncRNA DRAIC inhibits proliferation and metastasis of gastric cancer cells through interfering with NFRKB deubiquitination mediated by UCHL5.* Cell Mol Biol Lett, 2020. **25**: p. 29.
11. Rajasekaran, S., et al., *Non-coding and Coding Transcriptional Profiles Are Significantly Altered in Pediatric Retinoblastoma Tumors.* Front Oncol, 2019. **9**: p. 221.
12. Siegfried, N.A., et al., *RNA motif discovery by SHAPE and mutational profiling (SHAPE-MaP).* Nat Methods, 2014. **11**(9): p. 959-65.
13. Rice, G.M., C.W. Leonard, and K.M. Weeks, *RNA secondary structure modeling at consistent high accuracy using differential SHAPE.* RNA, 2014. **20**(6): p. 846-54.
14. Low, J.T. and K.M. Weeks, *SHAPE-directed RNA secondary structure prediction.* Methods, 2010. **52**(2): p. 150-8.
15. Ream, J.A., L.K. Lewis, and K.A. Lewis, *Rapid agarose gel electrophoretic mobility shift assay for quantitating protein: RNA interactions.* Anal Biochem, 2016. **511**: p. 36-41.
16. Hellman, L.M. and M.G. Fried, *Electrophoretic mobility shift assay (EMSA) for detecting protein-nucleic acid interactions.* Nat Protoc, 2007. **2**(8): p. 1849-61.
17. Rushe, M., et al., *Structure of a NEMO/IKK-associating domain reveals architecture of the interaction site.* Structure, 2008. **16**(5): p. 798-808.
18. Sparks, R.P., J.L. Jenkins, and R. Fratti, *Use of Surface Plasmon Resonance (SPR) to Determine Binding Affinities and Kinetic Parameters Between Components Important in Fusion Machinery.* Methods Mol Biol, 2019. **1860**: p. 199-210.
19. Jarmoskaite, I., et al., *How to measure and evaluate binding affinities.* Elife, 2020. **9**.
20. Schneider, C.S., et al., *Surface plasmon resonance as a high throughput method to evaluate specific and non-specific binding of nanotherapeutics.* J Control Release, 2015. **219**: p. 331-344.
21. Pijuan, J., et al., *In vitro Cell Migration, Invasion, and Adhesion Assays: From Cell Imaging to Data Analysis.* Front Cell Dev Biol, 2019. **7**: p. 107.
22. Jonkman, J.E., et al., *An introduction to the wound healing assay using live-cell microscopy.* Cell Adh Migr, 2014. **8**(5): p. 440-51.
23. Teng, L., et al., *The pan-cancer lncRNA PLANE regulates an alternative splicing program to promote cancer pathogenesis.* Nat Commun, 2021. **12**(1): p. 3734.
24. Solt, L.A. and M.J. May, *The IkappaB kinase complex: master regulator of NF-kappaB signaling.* Immunol Res, 2008. **42**(1-3): p. 3-18.

25. McFarlane, A.A., G.L. Orriss, and J. Stetefeld, *The use of coiled-coil proteins in drug delivery systems.* Eur J Pharmacol, 2009. **625**(1-3): p. 101-7.
26. Xia, Y., S. Shen, and I.M. Verma, *NF-kappaB, an active player in human cancers.* Cancer Immunol Res, 2014. **2**(9): p. 823-30.
27. Hoesel, B. and J.A. Schmid, *The complexity of NF-kappaB signaling in inflammation and cancer.* Mol Cancer, 2013. **12**: p. 86.
28. Hinz, M. and C. Scheidereit, *The IkappaB kinase complex in NF-kappaB regulation and beyond.* EMBO Rep, 2014. **15**(1): p. 46-61.
29. Liu, B., et al., *IKKalpha is required to maintain skin homeostasis and prevent skin cancer.* Cancer Cell, 2008. **14**(3): p. 212-25.
30. Zhao, D. and J.T. Dong, *Upregulation of Long Non-Coding RNA DRAIC Correlates with Adverse Features of Breast Cancer.* Noncoding RNA, 2018. **4**(4).
31. Guo, Q., et al., *NF-kappaB in biology and targeted therapy: new insights and translational implications.* Signal Transduct Target Ther, 2024. **9**(1): p. 53.
32. Verzella, D., et al., *Life, death, and autophagy in cancer: NF-kappaB turns up everywhere.* Cell Death Dis, 2020. **11**(3): p. 210.
33. Legarda-Addison, D., et al., *NEMO/IKKgamma regulates an early NF-kappaB-independent cell-death checkpoint during TNF signaling.* Cell Death Differ, 2009. **16**(9): p. 1279-88.
34. Nelson, G.W., S.A. Stohlman, and S.M. Tahara, *High affinity interaction between nucleocapsid protein and leader/intergenic sequence of mouse hepatitis virus RNA.* J Gen Virol, 2000. **81**(Pt 1): p. 181-8.
35. Chen, H., et al., *Mass spectroscopic characterization of the coronavirus infectious bronchitis virus nucleoprotein and elucidation of the role of phosphorylation in RNA binding by using surface plasmon resonance.* J Virol, 2005. **79**(2): p. 1164-79.
36. Shen, M., J. Rusling, and C.K. Dixit, *Site-selective orientated immobilization of antibodies and conjugates for immunodiagnostics development.* Methods, 2017. **116**: p. 95-111.
37. Hayden, M.S. and S. Ghosh, *Shared principles in NF-kappaB signaling.* Cell, 2008. **132**(3): p. 344-62.
38. Cappiello, F., B. Casciaro, and M.L. Mangoni, *A Novel In Vitro Wound Healing Assay to Evaluate Cell Migration.* J Vis Exp, 2018(133).
39. Przanowska, R.K., et al., *Distinct MUNC lncRNA structural domains regulate transcription of different promyogenic factors.* Cell Rep, 2022. **38**(7): p. 110361.
40. Busan, S. and K.M. Weeks, *Accurate detection of chemical modifications in RNA by mutational profiling (MaP) with ShapeMapper 2.* RNA, 2018. **24**(2): p. 143-148.
41. Smola, M.J., et al., *Selective 2'-hydroxyl acylation analyzed by primer extension and mutational profiling (SHAPE-MaP) for direct, versatile and accurate RNA structure analysis.* Nat Protoc, 2015. **10**(11): p. 1643-69.
42. Ponty, Y. and F. Leclerc, *Drawing and editing the secondary structure(s) of RNA.* Methods Mol Biol, 2015. **1269**: p. 63-100.
43. Arney, J.W. and K.M. Weeks, *RNA-Ligand Interactions Quantified by Surface Plasmon Resonance with Reference Subtraction.* Biochemistry, 2022. **61**(15): p. 1625-1632.
44. Harris, B.D., et al., *Human interferon-ϵ and interferon-kappa exhibit low potency and low affinity for cell-surface IFNAR and the poxvirus antagonist B18R.* J Biol Chem, 2018. **293**(41): p. 16057-16068.
45. Hwang, B., et al., *Quantification of cellular NEMO content and its impact on NF-kappaB activation by genotoxic stress.* PLoS One, 2015. **10**(3): p. e0116374.
46. Spriestersbach, A., et al., *Purification of His-Tagged Proteins.* Methods Enzymol, 2015. **559**: p. 1-15.

47. Ghandi, M., et al., *Next-generation characterization of the Cancer Cell Line Encyclopedia.* Nature, 2019. **569**(7757): p. 503-508.
48. Barretina, J., et al., *The Cancer Cell Line Encyclopedia enables predictive modelling of anticancer drug sensitivity.* Nature, 2012. **483**(7391): p. 603-7.
49. Kim, D., et al., *Graph-based genome alignment and genotyping with HISAT2 and HISAT-genotype.* Nat Biotechnol, 2019. **37**(8): p. 907-915.
50. Li, H., et al., *The Sequence Alignment/Map format and SAMtools.* Bioinformatics, 2009. **25**(16): p. 2078-9.

Table 1: A) LUAD tumors from TCGA classified by expression of 3-4a-4 junction vs 3-4 junction B) Eight matched tumors from the two subsets matched by equal expression of DRAIC, used for the heatmap of Fig. 7C.

A

LUAD classified by the expression of exon3-4a-4 and exon3-4

	exon 3-4a-4	**exon3-4**	**Total samples**
Subset A	yes	no	183
Subset B	no	yes	8

B

DRAIC expression in CPM

	Subset B (exon 3-4)	**Subset A (exon 3-4a-4)**
	Tumors 1-8	**Tumors 9-16**
Tumor 1, 9	0.38	0.38
Tumor 2, 10	3.92	3.92
Tumor 3, 11	0.83	0.82
Tumor 4, 12	3.83	3.91
Tumor 5, 13	0.69	0.67
Tumor 6, 14	0.56	0.55
Tumor 7, 15	0.36	0.36
Tumor 8, 16	0.41	0.41

CPM=count per million

Supplementary Table 1: The primers sequenced that are used in this study.

	Forward primer (5' to 3')	Reverse primer (5' to 3')
APTR (qPCR)	TGGCCATTTCCACATGTCAG	CTAGGCTCTTTCTTCATC
APTR (IVT)	TAATACGACTCACTATAGGGAGATGG CCATTTCCACATGTCAG	GTACACTTCACACCTGAACAC
A+B (qPCR)	TACCGAGCTCGGATC	ATAGGGCCCTCTAGATG
DRAIC (800-905)	CGCTCAACAACGAAAAGCAAAAAG	TTCATTAATGACACCTGATTTTGGAGG C
DRAIC (IVT 705-950)	TAATACGACTCACTATAGGGAGATTG GAATAACTTGCAG	CATTTCTTCAGAATTTTC
DRAIC (960-1105)	ATTTCCTGCTTTTCACAGAAAAC	ATGTTCATACTTCTGCTGCGTC
DRAIC (IVT FL)	TAATACGACTCACTATAGGGAGAC AGGGAGCTGGTTCCAGG	GACAGAGACGGAGAGATTTATTTT
GAPDH	AGGTCGGTGTGAACGGATTTG	TGTAGACCATGTAGTTGAGGTCA
Luciferase	ATGGAAGACGCCAAAAAC	CCTTATGCAGTTGCTCTCC
Luciferase (IVT)	TAATACGACTCACTATAGGGAGAATG GAAGATGCCAAAAACATTAAG	TTACACGGCGATCTTGCCGC

Supplementary Table 2: Sequences that are used to probe each exon.

exons	Probe sequence
Exon 3-4a-4	CTGAGGAACTTGGAATAACTTGCAGTGTCTTGCAGTATTG
Exon 3-4	ATGTGTAAACACTTGCTGAGTATTGTGAAACCAGCAACTT

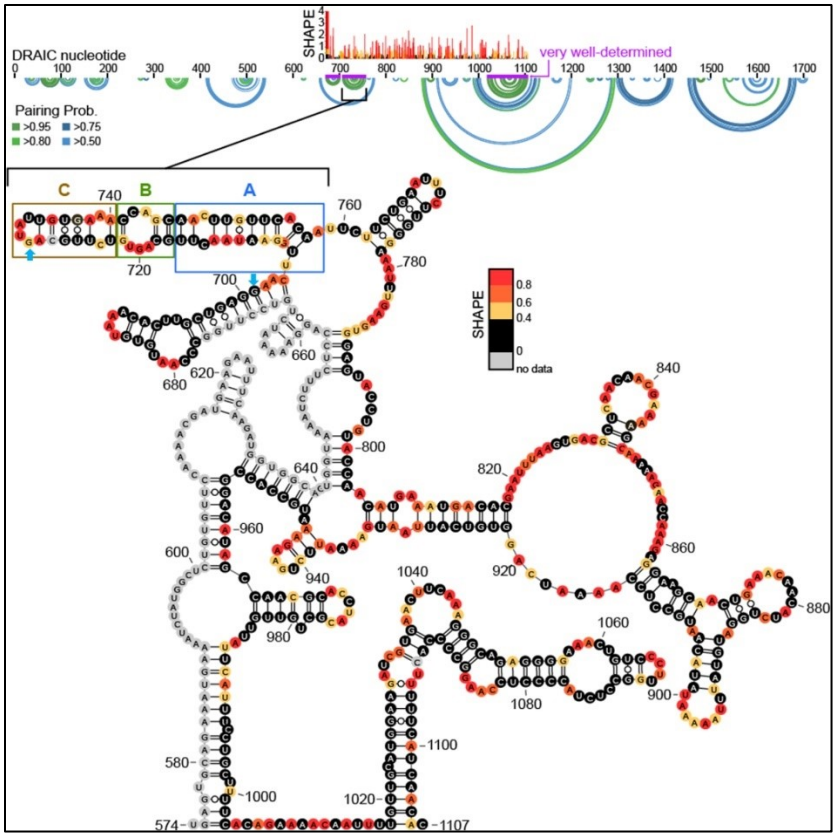

Fig. 1 Secondary Structure and SHAPE-MaP Analysis of functional DRAIC.

The secondary structure of the functional region of DRAIC, spanning nucleotides 574–1107, is illustrated with SHAPE reactivity data. SHAPE reactivity is shown as a color gradient from black (no data) to red (high reactivity, 0.8), indicating nucleotide flexibility. Notably, the region from 574–676 is computationally predicted to pair with corresponding regions. Regions of interest, including sections AB (nucleotides 705–722/741–758) and C (nucleotides 723–740), are highlighted with blue, green, and orange boxes, respectively. Pairing probabilities for various nucleotides are visualized using circular plots, with different levels (>0.50 in light green, >0.75 in dark green, >0.8 in light blue, and >0.95 in dark blue) shown in the corresponding rings. The purple-colored regions indicate well-determined structural areas, which include the locations of the ABC regions, highlighting their structural stability within the DRAIC sequence. The sequence between the blue arrowheads is the exon4a, that is excluded in some DRAIC isoform.

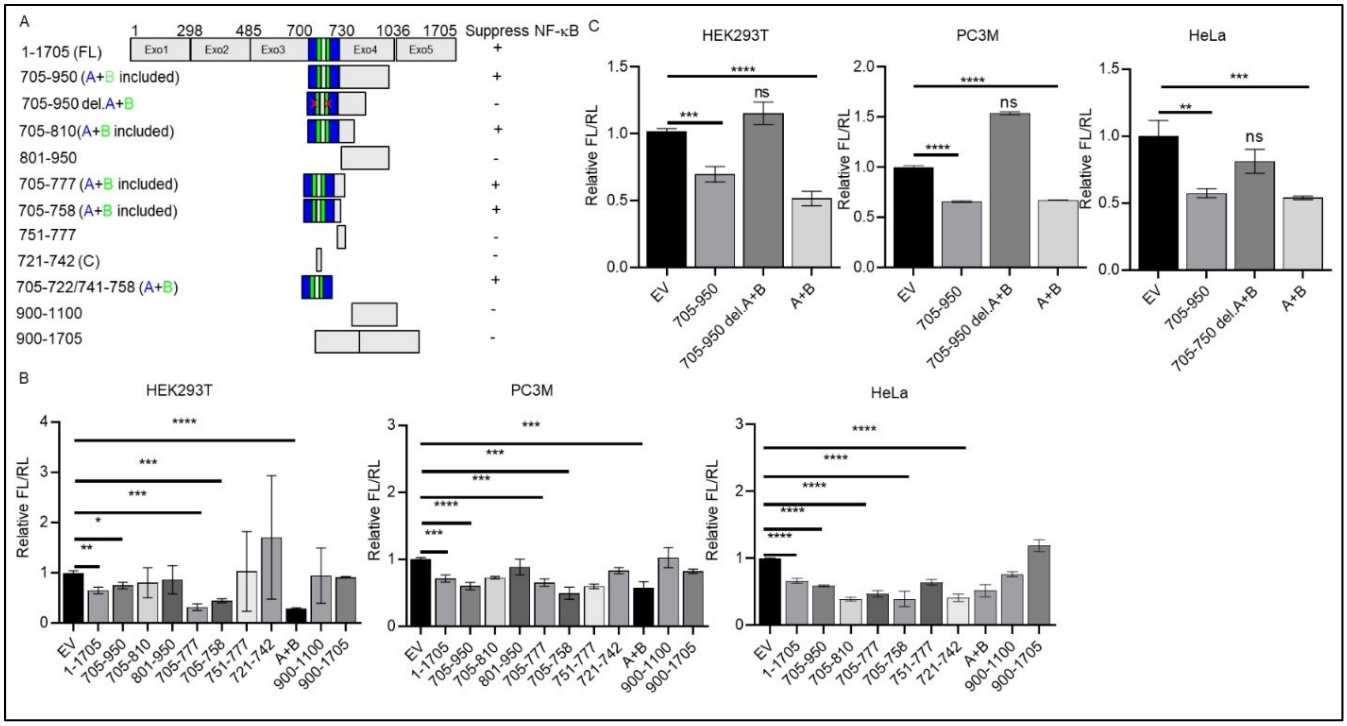

Fig. 2 36-bases contained in the A+B region of DRAIC is necessary and sufficient to inhibit NF-κB activity.

A Schematic of full-length DRAIC and deletion constructs and a summary of their ability to inhibit NF-κB driven luciferase reporter. The blue and green portions constitute A+B. "+" stands for inhibition of NF-κB activity. "-" stands for no inhibition effect on NF-κB activity.

B-C NF-κB driven luciferase reporter assay (Firefly luciferase/Renilla luciferase) in HEK293T, PC3M, and HeLa cells transfected with empty vector (EV) or plasmids overexpressing different portions of DRAIC. Data are expressed as mean ± SEM. *$P < 0.05$, **$P < 0.01$, ***$P < 0.001$, ****$P < 0.0001$ by One-tailed, unpaired Student *t*-tests (B) or by one-way ANOVA followed with Tukey correction (C). ns=no significant. In Figure 2B, only the significant comparisons are marked. Unmarked bars were not significantly different from the EV.

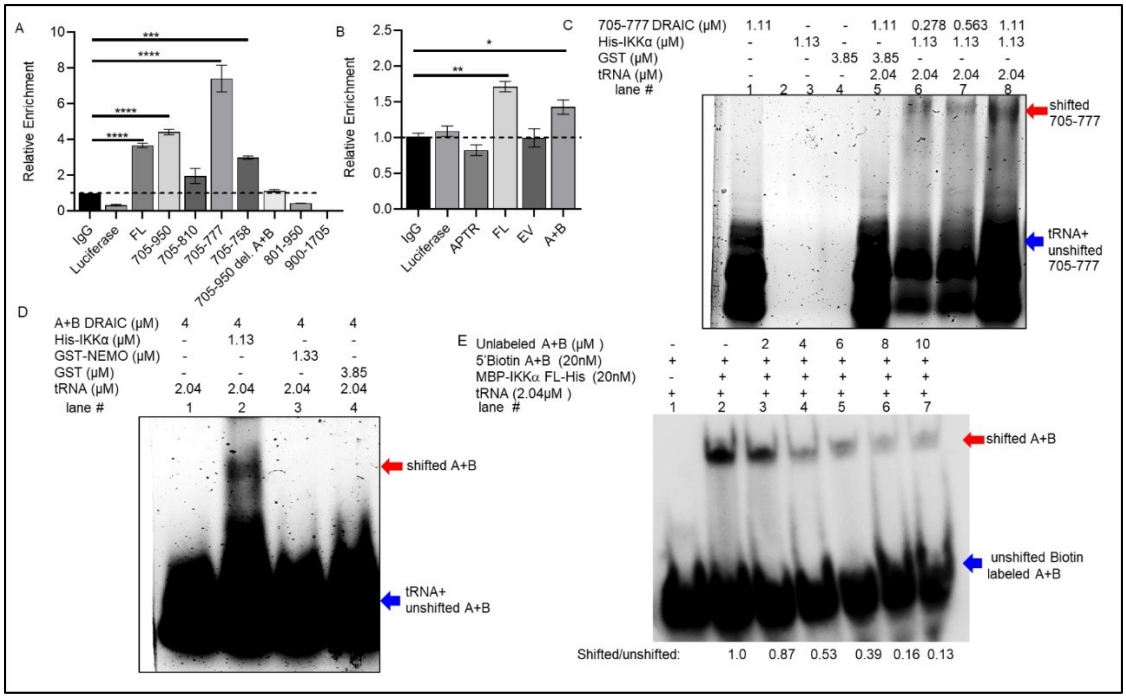

Fig. 3 Hairpin structure A+B specifically physically interacts with IKKα *in vitro*.

A-B In vitro–transcribed (IVT) DRAIC RNA fragments were incubated with recombinant IKK α protein and pulled down with IgG or IKK α antibody to see which portion of DRAIC interacts with IKK α protein. Luciferase RNAs, APTR lncRNA, and a short sequence from empty vector (EV) were used as negative controls. The relative enrichments were normalized to IgG.

C-D Electrophoretic mobility shift assays (EMSAs) to see if DRAIC (705-777) and A+B DRAIC RNAs were physically interact with IKKα protein. GST or GST-NEMO were used as negative controls. tRNAs were used as non-specific competitors. The red arrowhead indicates the protein-bound RNA ("shifted" RNA), blue arrowhead indicates the free RNA ("unshifted" RNA).

E Competitive EMSA was performed to see the specific interaction of A+B DRAIC RNA to IKK α protein. 5'Biotin labeled A+B DRAIC RNA was incubated with IKKα in the presence of unlabeled excess A+B DRAIC RNA as competitor. The arrowheads are the same as in **C-D**. The numbers at the bottom of the image are the ratio of shifted to unshifted RNAs which is normalized to lane #2. Data are expressed as mean ± SEM. *$P < 0.05$, **$P < 0.01$, ***$P < 0.05$, ***$P < 0.0001$ by One-tailed, unpaired Student *t*-tests (B and C).

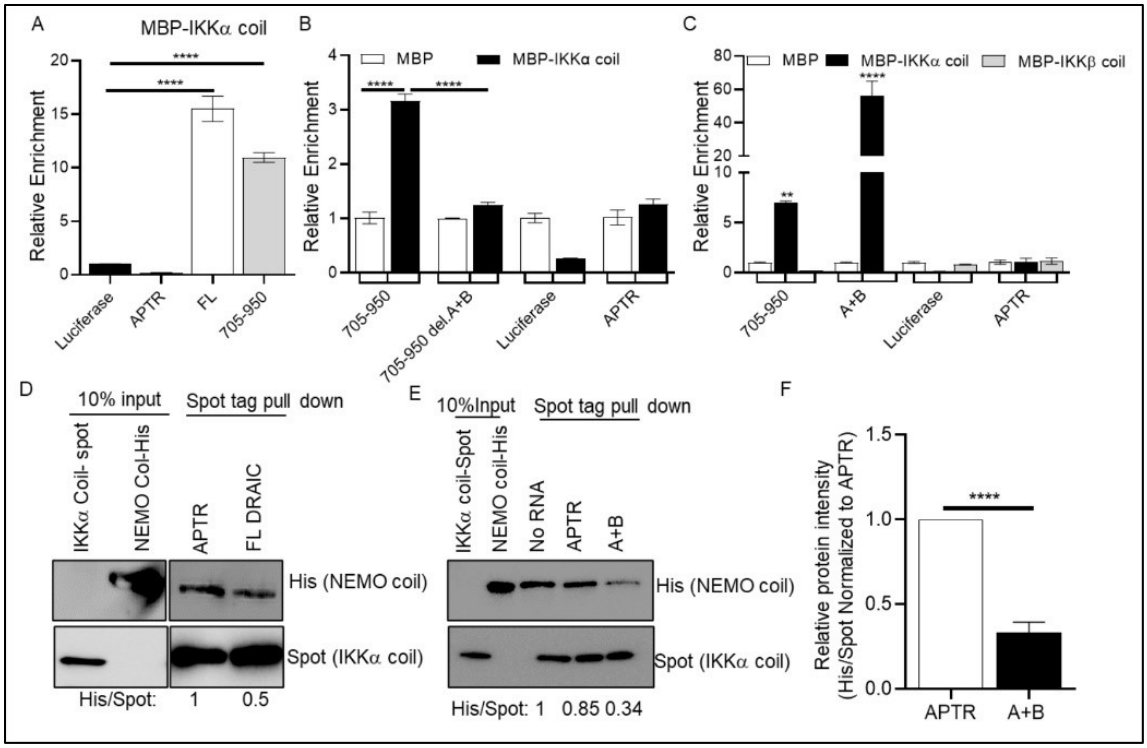

Fig. 4 Hairpin structure A+B specifically physically interacts with IKKα coiled-coil domain.

A-C RIP to detect if FL DRAIC and indicated parts interact with IKKα coiled-coil domain. Luciferase and APTR lncRNA were used as negative controls. MBP tag only and MBP-IKKβ coiled-coil domain protein were also included as negative controls.

D-E In vitro IKK complex formation assay to see if the binding of FL DRAIC (D) and A+B DRAIC (E) to IKKα coiled-coil domain affects the binding of NEMO to IKKα. IKKα coiled-coil protein was immobilized on Spot magnetic beads, then FL DRAIC RNA or A+B DRAIC RNA and His- NEMO coiled-coil protein were introduced. Proteins associated with the Spot beads are visualized by Western blotting.

F The quantification of the relative protein intensity of Spot (IKKα coiled-coil) and His (NEMO coiled-coil) in the presence of APTR and A+B DRAIC RNA. Data are expressed as mean ± SEM of 6. $^{**}P < 0.01$, $^{***}P < 0.05$, $^{****}P < 0.0001$ by one-way ANOVA followed with Tukey correction (A), two-way ANOVA followed with Tukey correction (B and C) or by one-tailed, unpaired Student *t*-tests (F).

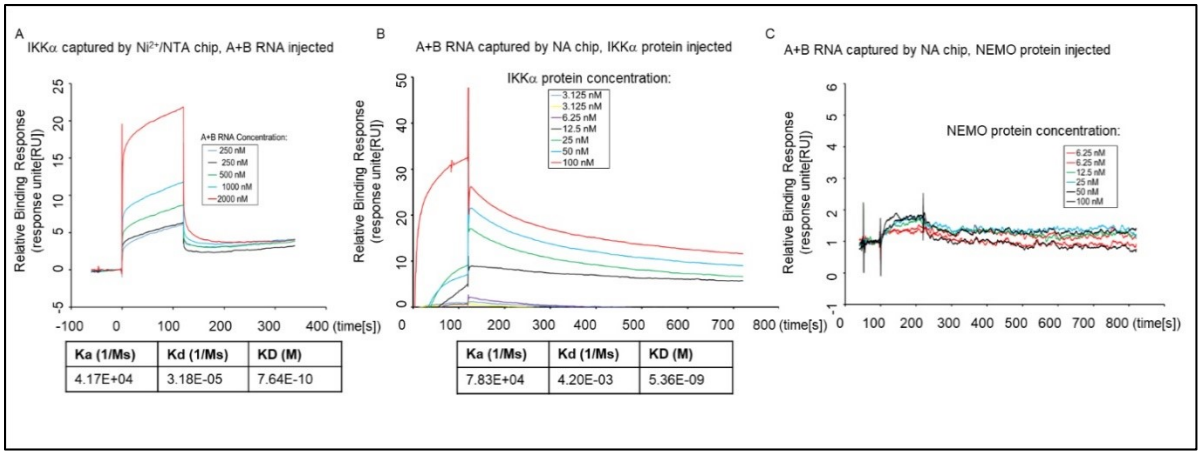

Fig. 5 High binding affinity of A+B to IKKα measured by Surface Plasmon resonance.

A His6-tagged IKKα was immobilized on the sensor chip using Ni^{2+}/NTA chip, and doses of A+B RNAs injected. The table at the bottom of the sensorgram shows the kinetic parameters that are on-rate K_a and an off-rate K_d and the calculated K_D (K_d/ K_a) based on 1:1 steady binding model.

B 5'Biotin-A+B RNA was immobilized on the sensor surface by NA (Neutravidin) chip, and doses of MBP-IKK α-His protein were injected in solution as the analyte. All the experiments were conducted at 25°C.

C Similar to B, doses of GST-NEMO protein were injected over the sensor chip after 5'Biotin-A+B RNA was immobilized.

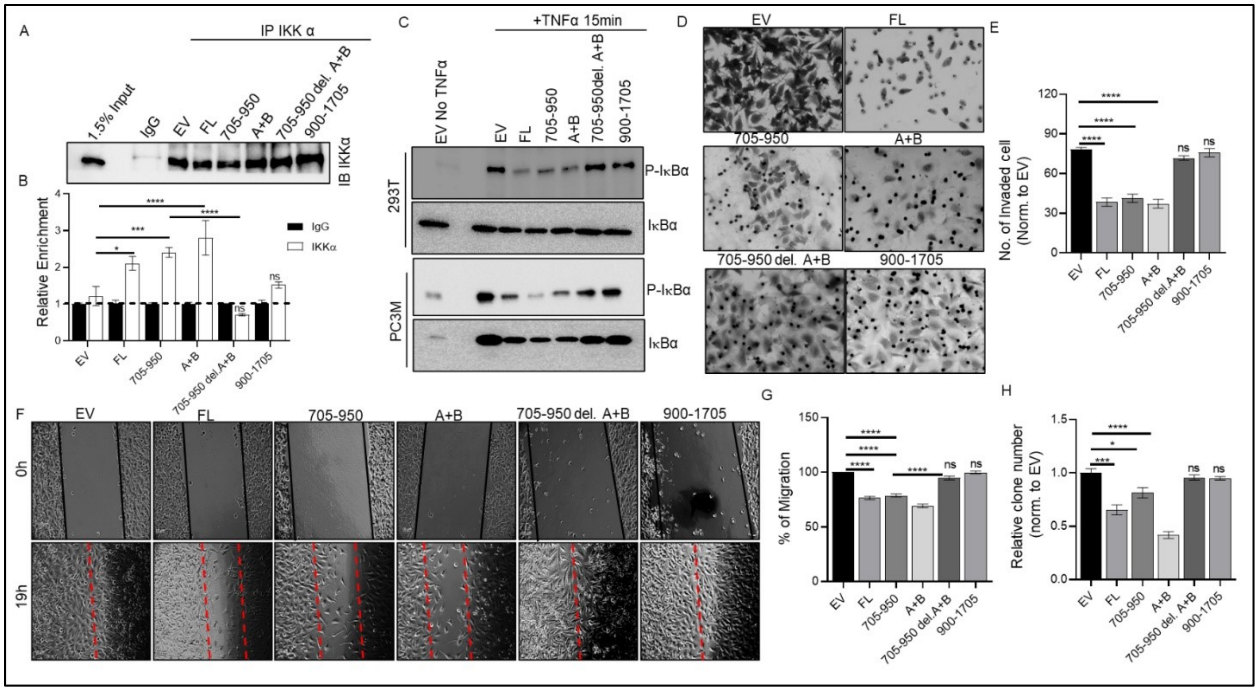
A
IP IKK α
1.5% Input
IgG
EV
FL
705-950
A+B
705-950 del. A+B
900-1705
IB IKKα
B
Relative Enrichment
IgG
IKKα
EV
FL
705-950
A+B
705-950 del.A+B
900-1705
C
+TNFα 15min
EV No TNFα
EV
FL
705-950
A+B
705-950del. A+B
900-1705
293T
PC3M
P-IκBα
IκBα
D
EV
FL
705-950
A+B
705-950 del. A+B
900-1705
E
No. of Invaded cell (Norm. to EV)
F
EV
FL
705-950
A+B
705-950 del. A+B
900-1705
0h
19h
G
% of Migration
H
Relative clone number (norm. to EV)

Fig. 6 A+B binds to IKKα and inhibits the phosphorylation of IκBα, suppresses cancer cells migration, invasion and clonogenic formation when expressed in cells.

A-B RIP was performed after overexpression of FL DRAIC and DRAIC derivatives to see if A+B part of DRAIC interacting with IKKα in vivo. (A) Immunoblotting of IKKα in the immunoprecipitates showing equal pull down of the protein. (B) RT-qPCR showing the relative enrichment to IKKα (normalized to IgG).

C Western blotting was performed to detect the phosphorylation levels of IκBα after overexpressing DRAIC derivatives in HEK293T (upper panel) and PC3M (lower panel). Loading controls were used to adjust the equal amount of protein loaded.

D Matrigel Invasion assay was conducted in PC3M cells after transfection with FL DRAIC and DRAIC derivatives to see if A+B affects tumor cell invasion. The scale bar is 50 μm.

E Quantitation of the invaded cells from D.

F Wound Healing assay was performed to evaluate if A+B affects PC3M cell migration after DRAIC transfection. The dotted lines define the areas lacking cells. The scale bar is 10 μm.

G Quantitation of the wound closure from F, normalized to the closure with EV.

H Quantitation of the colony number after DRAIC in Clonogenicity assay to see if A+B affects PC3M cell clonogenic growth on plastic tissue culture plate. Cells were fixed and stained with 0.5% Crystal Violet. Data are expressed as mean ± SEM of 2 replicate; 4-5 random fields captured for each replicates; $^{*}P < 0.05$, $^{***}P < 0.001$, $^{****}P < 0.0001$ by one-way or two-way ANOVA followed with Tukey correction. ns= not significant when compared to EV.

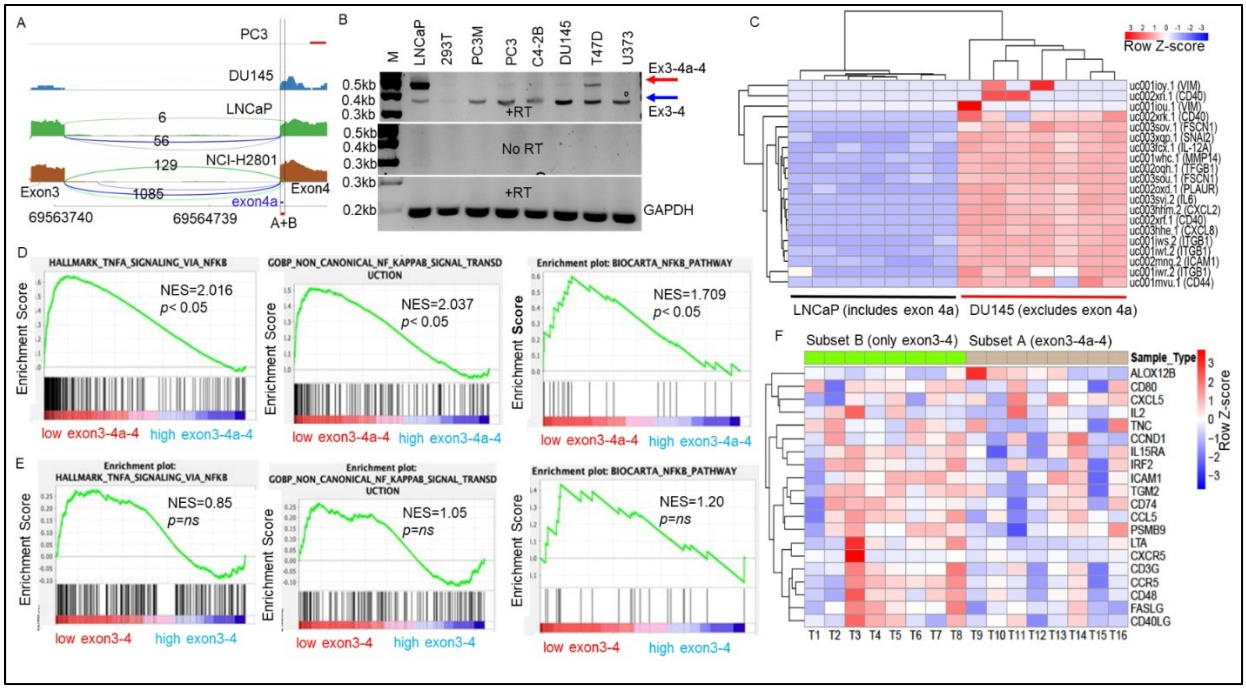
A
PC3
DU145
LNCaP
6
56
129
NCI-H2801
1085
Exon3
Exon4
exon4a
69563740
69564739
A+B
B
M
LNCaP
293T
PC3M
PC3
C4-2B
DU145
T47D
U373
Ex3-4a-4
Ex3-4
0.5kb
0.4kb
0.3kb
+RT
No RT
0.2kb
GAPDH
C
Row Z-score
LNCaP (includes exon 4a)
DU145 (excludes exon 4a)
D
HALLMARK_TNFA_SIGNALING_VIA_NFKB
NES=2.016
p< 0.05
GOBP_NON_CANONICAL_NF_KAPPAB_SIGNAL_TRANSDUCTION
NES=2.037
p< 0.05
Enrichment plot: BIOCARTA_NFKB_PATHWAY
NES=1.709
p< 0.05
Enrichment Score
low exon3-4a-4
high exon3-4a-4
E
Enrichment plot: HALLMARK_TNFA_SIGNALING_VIA_NFKB
NES=0.85
p=ns
Enrichment plot: GOBP_NON_CANONICAL_NF_KAPPAB_SIGNAL_TRANSDUCTION
NES=1.05
p=ns
Enrichment plot: BIOCARTA_NFKB_PATHWAY
NES=1.20
p=ns
low exon3-4
high exon3-4
F
Subset B (only exon3-4)
Subset A (exon3-4a-4)
Sample_Type
ALOX12B
CD80
CXCL5
IL2
TNC
CCND1
IL15RA
IRF2
ICAM1
TGM2
CD74
CCL5
PSMB9
LTA
CXCR5
CD3G
CCR5
CD48
FASLG
CD40LG
T1 T2 T3 T4 T5 T6 T7 T8 T9 T10 T11 T12 T13 T14 T15 T16
Row Z-score

Fig. 7 Alternative splicing regulates the ability of DRAIC to inhibit NF-κB signaling in cancer cell lines and in LUAD tumor.

A The sashimi plot of RNA-seq data illustrates the alternative splicing event involving exon 4a in DRAIC across various cell lines. The lines connecting exon 3 and exon 4 represent splicing events, either directly between exon 3 and exon 4 (green line) or through the inclusion of exon 4a (blue line). The numbers along the lines indicate the frequency of these splicing events. The red-colored region highlights the A+B segment, with the blue-colored region specifically marking exon 4a. The numbers at the bottom denote the chromosomal loci on chromosome 15.

B RT-PCR analysis showing the relative abundance of DRAIC transcripts with and without Exon 4a in several cell lines. RT=reverse transcription. M stands for DNA marker.

C Heatmap showing downregulation of NF-κB-regulated inflammatory genes in LNCaP cells expressing exon 4a compared to DU145 cells lacking exon 4a. The scale represents the Row Z-score.

D GSEA highlighting NF-κB-regulated inflammatory genes enriched in LUAD tumors in TCGA with low exon 3-4a-4 expression (Q1) compared to those with high exon 3-4a-4 expression (Q4). NES=Normalized enrichment score. $P<0.05$ is statistically significant.

E GSEA shows that NF-κB-regulated inflammatory enriched genes are not differentially enriched in LUAD tumors with low (Q1) or high (Q4) expression of exon3-4 isoform of DRAIC.

F The heatmap illustrates NF-κB target gene expression in eight LUAD tumors matched by expression of DRAIC but expressing or not expressing exon 4a (from Table 1). NF-κB targets are upregulated in tumors expressing exon 3-4 compared to those expressing exon 3-4a. The scale represents the Row Z-score.

Supplementary Figure legends

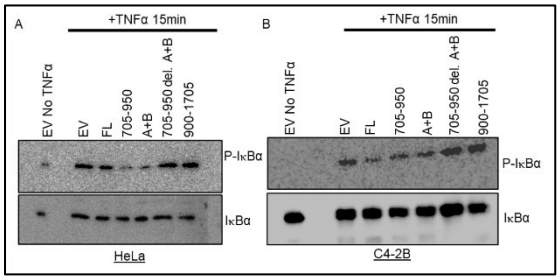

Fig. S1 A+B inhibits the phosphorylation of IκBα in HeLa and C4-2B cell lines.

A and B Western blotting was performed to detect the phosphorylation levels of IκBα after overexpressing DRAIC derivatives in HeLa cells (A) and C4-2B (B). Loading controls were used to adjust the equal amount of protein loaded.

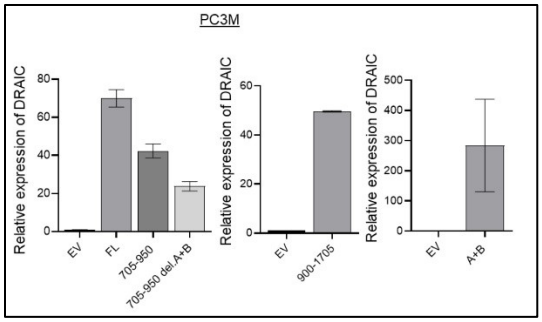

Fig. S2 Overexpressing different portions of DRAIC in PC3M cell confirmed by RT-qPCR

RT-qPCR measures the level of DRAIC after overexpressing different portions of DRAIC in PC3M cells. Primer sequences provided in the Supplemental Table1.

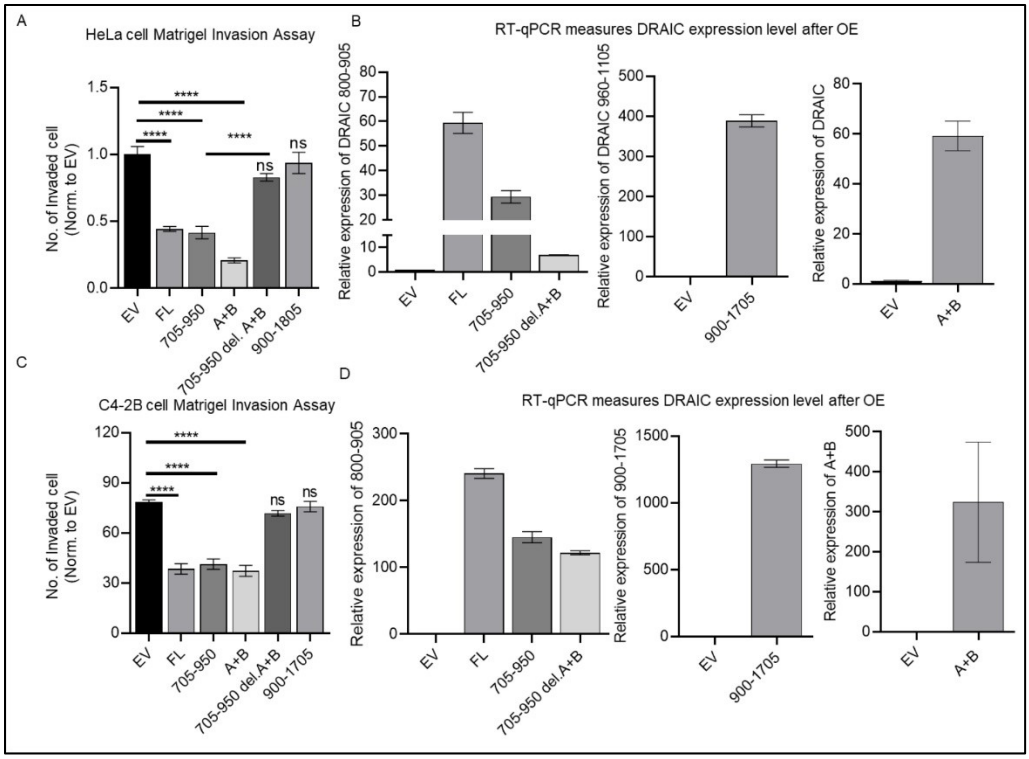

Fig.S3 A+B inhibits migration in HeLa and C4-2B cancer cells.

A and C Matrigel Invasion assay was conducted in HeLa (A) and C4-2B (C) cells after transfection with FL DRAIC and DRAIC derivatives to see if A+B affects tumor cell invasion. The invaded cells were quantified.

B and D RT-qPCR measures the level of DRAIC after overexpressing different portions of DRAIC in HeLa (B) and C4-2B (D) cancer cells. Data are expressed as mean ± SEM of 7-8; ****$P < 0.0001$ by one-way ANOVA followed with Tukey correction. ns= no significant when compared to EV.